

Measuring the seismic velocity in the top 15 km of Earth's inner core

Harriet Godwin^{a,*}, Lauren Waszek^{b,c}, Arwen Deuss^d

^a*University of Oxford, Department of Earth Sciences, South Parks Road, Oxford OX1 3AN, United Kingdom*

^b*Australian National University, Research School of Earth Sciences, 142 Mills Road, Acton, ACT 2601, Australia*

^c*New Mexico State University, Department of Physics, 1255 North Horseshoe, Las Cruces, NM 88003, United States*

^d*Utrecht University, Department of Earth Sciences, PO Box 80125, 3508 TC Utrecht, The Netherlands*

Abstract

We present seismic observations of the uppermost layer of the inner core. This was formed most recently, thus its seismic features are related to current solidification processes. Previous studies have only constrained the east-west hemispherical seismic velocity structure in the Earth's inner core at depths greater than 15 km below the inner core boundary. The properties of shallower structure have not yet been determined, because the seismic waves PKIKP and PKiKP used for differential travel time analysis arrive close together and start to interfere. Here, we present a method to make differential travel time measurements for waves that turn in the top 15 km of the inner core, and measure the corresponding seismic velocity anomalies. We achieve this by generating synthetic seismograms to model the overlapping signals of the inner core phase PKIKP and the inner core boundary phase PKiKP. We then use a waveform comparison to attribute different parts of the signal to each phase. By measuring the same parts of the signal in both observed and synthetic data, we are able to calculate differential travel time residuals. We apply our method to data with ray paths which traverse the Pacific hemisphere boundary. We generate a velocity model for this region, finding lower velocity for deeper, more easterly ray paths. Forward modelling suggests that this region contains either a high velocity upper layer, or variation in the location of the hemisphere boundary with depth and/or latitude. Our study presents the first direct seismic observation of the uppermost 15 km of the inner core, opening new possibilities for further investigating the inner core boundary region.

Keywords: Seismology, body waves, inner core

1. Introduction

The structure of Earth's inner core remains much less constrained than its mantle. The solid inner core is composed of an iron-nickel alloy, with an unknown quantity of light elements (Antonangeli et al., 2010). As the Earth cools, material from the liquid outer core crystallises onto the surface of the inner core at a rate of about 0.3 mm/year (Jacobs, 1953; Labrosse et al., 2001; Aubert et al., 2008). This process releases latent heat and light elements which

*Corresponding author

6 drive convection in the outer core, and ultimately the geodynamo. The properties of the inner core are determined
7 by the conditions at the inner core boundary (ICB) at the time of freezing. Consequently, the thermal history of the
8 ICB is recorded in the seismic structure of the inner core. The very uppermost layer of the inner core is therefore of
9 particular importance, as it is linked to the most recent conditions of the ICB and the current state of the geodynamo.
10 However, direct measurements of velocity properties within this layer have not yet been made. This is because at
11 depths shallower than 15 km below the ICB, the seismic phases PKIKP and PKiKP used to observe it arrive at very
12 similar times and interfere.

13 The seismic velocity structure of the inner core is highly complex. Studies have shown evidence of anisotropy, ori-
14 ented with the fast direction aligned to Earth's rotation axis (Poupinet et al., 1983; Morelli et al., 1986; Woodhouse et al.,
15 1986; Creager, 1992; Vinnik et al., 1994; Irving & Deuss, 2011). A distinct east-west asymmetry has also been ob-
16 served in the inner core, whereby the west hemisphere has lower velocity, weaker attenuation and stronger anisotropy
17 than the east (Tanaka & Hamaguchi, 1997; Niu & Wen, 2001; Cao & Romanowicz, 2004; Oreshin and Vinnik, 2004;
18 Deuss et al., 2010; Waszek et al., 2011). The difference in isotropic velocity between the hemispheres has been found
19 to be between 0.5% (Sun & Song, 2008) and 1.5% (Garcia, 2002), with most studies finding a value of 0.8% -
20 1% (Tanaka & Hamaguchi, 1997; Niu & Wen, 2001; Cao & Romanowicz, 2004). The hemisphere boundaries have
21 been observed as sharp (Waszek & Deuss, 2011), and may vary with depth in the inner core (Waszek et al., 2011).
22 Further irregularities and variation in the location of the Pacific boundary have been observed (Miller et al., 2013;
23 Irving & Deuss, 2015; Yu et al, 2017). Small scale features on the inner core boundary have been detected in this area
24 (Waszek & Deuss, 2015; Tian & Wen, 2016; Shen et al., 2016), which may be linked to regional solidification of the
25 inner core (Cormier, 2015).

26 Two contrasting geodynamical models have been suggested to explain the hemispherical structure. In the first
27 model, the inner core is coupled to thermal structure at the core-mantle boundary. This results in variations in heat flux
28 at the ICB, and produces a hemispherical difference in the freezing rate of the inner core (Aubert et al., 2008). The
29 difference in growth rate is then linked to the seismic properties. In the second model, a lateral eastward translation of
30 the inner core is driven by crystallisation in the west and melting in the east (Monnereau et al., 2010; Alboussière et al.,
31 2010). This produces older structure in the east hemisphere, with a corresponding difference in seismic properties.
32 Neither of the two mechanisms can fully explain the seismic observations, especially regional and depth variations.

33 In order to better understand the origin of the observed structure, we must constrain the properties of the most
34 recently formed material at the top of the inner core. Previous inner core studies have obtained the seismic velocity by
35 using differential travel time measurements of the body waves PKIKP and PKiKP. PKIKP travels into the inner core,
36 and PKiKP is a reference phase which reflects from the inner core boundary (Figure 1). When PKIKP travels deeper
37 into the inner core, the phases arrive separately and can be distinguished easily. However, as the PKIKP and PKiKP
38 paths become more similar at shallow inner core depths, the signals arrive closer together. At an epicentral distance

of around 130° , which corresponds to 15 km below the inner core boundary, the signals begin to overlap. At shorter distances, and shallower depths, it is no longer straightforward to separate and identify the phases. Previously, structure in the uppermost region of the inner core has been investigated using waveform modelling of synthetic seismograms (Wen & Niu, 2002; Stroujkova & Cormier, 2004). However, travel time measurements of the phases within the upper 15 km of the inner core have not yet been made.

Here, we make direct observations of the seismic velocity structure of the upper 15 km of the inner core, by using waveform modelling for the phases. We generate synthetic seismograms for individual PKIKP and PKiKP phases, in order to identify features in the observed data which correspond to each phase. By selecting the corresponding features in the observed and synthetic data, we measure differential travel times in both data sets to obtain a residual. This technique does not require us to use the same part of the waveform for each phase, which is essential for the cross-correlation technique previously used for picking. As a benchmark, at larger epicentral distances we also measure the residuals using cross-correlation. For proof of concept, we apply this technique to an event in Indonesia on 15 November 2011, received at the US Array. We then collect data from 11 other events in the region. The ray paths traverse the inner core through the Pacific hemisphere boundary. We make differential travel time residual measurements, and subsequently calculate a layered seismic velocity model for this region. Finally, we forward model two potential velocity structures.

2. Method and data

2.1. Method

The compressional wave velocity in the inner core is determined by measuring the difference in travel time between two seismic phases, PKIKP and PKiKP. The inner core phase PKIKP travels through the mantle, outer core and inner core. The reference phase PKiKP follows a very similar path through the mantle and outer core, but reflects at the ICB (Figure 1). Consequently, the difference in their arrival times is related to the velocity structure in the upper inner core. The observed PKIKP-PKiKP differential travel time is compared to that predicted from a reference Earth model; here, we use the 1D Earth model AK135 (Kennett et al., 1995) for its updated outer core structure with respect to PREM.

The PKIKP-PKiKP differential travel time residual, δt , is defined as follows:

$$\delta t = (t_{PKiKP} - t_{PKIKP})_{observed} - (t_{PKiKP} - t_{PKIKP})_{AK135} \quad (1)$$

where t_{PKIKP} and t_{PKiKP} are the travel times of the respective phase. Due to higher compressional velocity in the inner core than the outer core, PKIKP arrives before PKiKP. A positive residual means that PKIKP arrives earlier than expected with respect to PKiKP. Consequently, it is associated with higher seismic velocities along the PKIKP path in the inner core than predicted by AK135. Conversely, a negative residual corresponds to lower seismic velocities than AK135.

69 We calculate the inner core ray paths and arrival times using the TauP toolkit (Crotwell et al., 1999) with AK135
70 (Kennett et al., 1995). The hemisphere boundary of 173°W defined by Waszek et al. (2011) in the upper inner core
71 suggests that the paths primarily traverse the eastern hemisphere. The higher isotropic velocity here should result in
72 larger differential travel times, therefore we can use shorter epicentral distances than for the western hemisphere. We
73 select rays travelling in the same direction through the inner core to eliminate the influence of anisotropy. This allows
74 us to better track the moveout of the phases with epicentral distance, which is extremely useful for phase identification
75 at short epicentral distances.

76 For making differential measurements, we generate theoretical seismograms using the high frequency WKBJ
77 approximation (Chapman, 1976), which produces synthetic data in a 1D model for specific phases; this feature is
78 integral to the method. The focal mechanisms are obtained from the Global CMT Catalog (Ekström et al., 2012).
79 Source-time functions are calculated for each event with P-wave data in the 30 – 90° epicentral distance range, using
80 the technique previous applied to inner core data by Garcia (2002). We firstly remove the instrument response, and
81 integrate the seismograms to displacement. The data are filtered between 0.2 – 1.0 Hz to remove microseismic and
82 high frequency noise, and then quality checked. Finally, we normalise the P-wave peaks to remove radiation effects,
83 and take their average to obtain the source-time functions (Figure S1). A global average of data is used, to suppress
84 regional structure. Due to the small azimuth range of our data, a requirement of the technique, we do not model
85 azimuthal variation in the source time functions.

86 Synthetics are calculated for PKIKP and PKiKP individually (“single-phase” synthetics), and for combined PKIKP-
87 PKiKP phases (“two-phase” synthetics). All are convolved with the event-specific source-time function. The single-
88 phase synthetic waveforms are used to identify peaks corresponding to each phase. Using these peaks, synthetic
89 differential travel times are measured on the two-phase synthetics. The corresponding peaks are then located in the
90 observed data, and their differential time measured. Subsequently, we obtain a differential travel time residual. The
91 same data processing methods, outlined below, are applied to both the real and synthetic data sets prior to picking.

92 2.2. Data

93 We use vertical component seismic data from 12 earthquakes located in south east Asia, received at the US array
94 (Table 1). All data were obtained from the IRIS-DMC digital dataset. The earthquake locations are constrained by
95 our method’s requirement for a large, dense configuration of seismic stations in the epicentral distance range 125 –
96 135° from the earthquake. Focal depths greater than 15 km prevent interference from surface reflections, and help to
97 remove source-side crustal reverberations and attenuation effects in the upper mantle and crust. We also require that
98 the event has a magnitude large enough to be observed, but with an impulsive mechanism since the phases arrive close
99 together, corresponding to a range of m_b values from 5.3 to 6.3 (Table 1). Consequently, several candidate earthquakes
100 were discarded due to long source time functions and broad waveforms. As proof of concept, we use data from the 15

101 November 2011, m_b 5.7 Indonesia event (Figure 2), which has by far the largest number of seismograms. Our final
102 dataset comprises 252 seismograms from this earthquake, and 986 from the other 11 events, giving a total of 1237
103 data.

104 We first filter the data at frequencies from 0.7 to 2.0 Hz. This filter focuses on the main PKIKP frequency of 1.0
105 Hz, while also removing higher frequency PKP precursors (Cormier, 1999), and the low frequency PKP-B caustic
106 (Thomas et al., 2009). The data are then quality checked to remove noisy signals and outlying ray paths. For the
107 Indonesian event, this leaves 251 seismograms from an original total of 348. We then normalise the seismograms
108 on the largest amplitude peak of PKiKP. Figure 3 shows the resultant seismograms for observed and synthetic data
109 respectively. The influence of regional mantle velocity structure is clear for the observed data, and hence we align the
110 seismograms on the PKiKP phase to remove this effect.

111 Epicentral distance is a proxy for PKIKP turning depth in the inner core, whereby a shorter distance corresponds
112 to a shallower PKIKP turning depth. As epicentral distance decreases, PKIKP and the reference phase PKiKP begin
113 to overlap. Examples of individual seismograms at 125.6° and 134.7° are shown in Figure 4. It is comparatively
114 straightforward to identify the phases for larger distances as demonstrated in previous studies (Figure 4b). At 134.7° ,
115 we have indicated the PKIKP and PKiKP peaks which would be picked using cross-correlation techniques. At shorter
116 distances we cannot separate the phases in an individual seismogram, and therefore require an alternative method to
117 measure the travel time difference (Figure 4a). Arrows indicate the peaks which we use to identify the phases in our
118 study.

119 For our data, we determine that it is impossible to extract information for source-station distances below about
120 125° , corresponding to just 6 km depth below the ICB. We therefore analyse data with distances from $125 - 130^\circ$, to
121 provide new constraints on the uppermost layer at 6 – 15 km below the ICB. We also analyse data from $130 - 135^\circ$, to
122 compare our results with previous observations (Waszek & Deuss, 2011) and verify our method.

123 3. Results

124 3.1. Synthetic seismograms

125 Previous studies measured the PKIKP-PKiKP differential travel time residual in individual seismograms using a
126 combination of cross-correlation and hand-picking (e.g. Waszek & Deuss, 2011). At distances larger than 130° the
127 phases arrive separately, with approximately opposite polarity due to the reflection of PKiKP at the ICB (Figure 4b).
128 However, when the phases are observed at epicentral distances below 130° , it is not possible to use these methods for
129 identification and measurement. As epicentral distance decreases, the paths travelled by the PKIKP and PKiKP rays
130 become very close. The similarity in the paths is reflected in the shape of the waveforms where, instead of a reversal
131 in polarity between phases, relative changes in amplitude of peaks are observed (Figure 4a). The close ray paths also

means that the phase signals overlap. The first arrival of PKiKP interferes with the second peak of PKIKP, meaning a PKIKP-PKiKP differential travel time cannot easily be measured.

To solve this problem, we compare the observed data with the synthetic seismograms to assign peaks in the observed seismograms to PKIKP and PKiKP. Here, the characteristic peak of PKIKP does not correspond to the same peak for PKiKP, as is required by cross-correlation. In other words, we do not measure the first peak for both phases, or the second peak for both phases. Instead, we use synthetics calculated for PKIKP and PKiKP individually to identify a peak in the observed data which is attributed to each phase. This means, for example, that we pick the first peak of PKIKP, and the second peak of PKiKP. The times of these peaks are taken as the arrival times of each phase. We then generate combined PKIKP-PKiKP synthetics, and measure the same peaks to obtain the predicted differential time. While this is larger than a true differential travel time, using different parts of the waveform does not affect the differential travel time residual so long as we make the same measurement in the synthetic data. As a result, we are able to generate PKIKP-PKiKP differential travel time residuals, despite not measuring actual PKIKP-PKiKP differential times in the data. This method is valid as long as PKiKP does not interfere with the first peak of PKIKP.

3.2. Alignment and measurement

We align the observed and synthetic seismograms on a peak from the PKiKP phase, which corresponds to the largest amplitude peak on the seismogram. The aligned seismograms are shown as a function of epicentral distance in Figures 5 and 6 for $125 - 130^\circ$ and $130 - 135^\circ$ respectively. PKIKP arrives before PKiKP, with a different, more positive slowness, observed as the increase in differential travel time with epicentral distance. The synthetic seismograms correspond to a theoretical 1D Earth structure of model AK135, and therefore are aligned on the PKiKP theoretical travel time. The phase shift of PKiKP increases from approximately $110 - 140^\circ$ in our epicentral distance range (Cao & Romanowicz, 2006), which is observed as a small shift in the earlier part of the PKiKP waveform as distance increases. Thus, we align on the second peak due to its consistent shape.

Examination of the synthetic seismograms allows features of the real seismograms to be associated with either the PKIKP or PKiKP phase. We mark the characteristic peaks selected for each phase in Figures 5 and 6. In the $125 - 130^\circ$ distance range, Figure 5d shows that the PKiKP waveform is characterised by the large peak at a relative travel time of 0 s. This is the peak chosen for alignment. To constrain PKIKP, we examine Figure 5c. Here, PKIKP arrives at a different slowness to PKiKP, moving out with increasing epicentral distance. We find that PKIKP has a waveform characterised by a peak-trough-peak pattern, and we select the first peak of PKIKP as the characteristic peak. The combination of the two phases in Figure 5b reveals that the peak which appears at larger epicentral distances between the arrival of PKIKP and PKiKP is the result of interference between the two phases.

The line indicating the PKIKP arrival time in Figures 5 and 6 represents the line of best fit of the PKIKP arrival times. To calculate this, we measure the relative arrival of the PKIKP peak in each PKIKP-PKiKP seismogram

164 by using cross-correlation with the PKiKP peak. Unlike the previous cross-correlation picking methods, here we
165 cross-correlate for peaks of the same polarity. We then determine the line of best fit using a least squares regression
166 (Williams & Kelley, 2011). The good fit of this line confirms the correspondence between the peak marked and the
167 arrival of PKiKP.

168 In the $130 - 135^\circ$ epicentral distance range, we again show the arrival of PKiKP with a red line (Figure 6). Here,
169 the first of the PKiKP peaks is also used to mark its arrival, since it is easier to identify and less likely to be masked by
170 the larger PKiKP arrival. As before, this does not correspond to a true differential travel time. We pick the same peaks
171 in the synthetics to obtain correct residuals. Data in this epicentral distance range are usually picked using peaks of
172 the opposite polarity (Niu & Wen, 2001; Cao & Romanowicz, 2004; Waszek & Deuss, 2011). For comparison, in this
173 distance range we also measure our data using cross-correlation of the opposite polarity peaks, to confirm the validity
174 of our method.

175 *3.3. Differential travel times*

176 Figure 7 shows the measured PKiKP and PKiKP differential travel times for observed and synthetic data as a
177 function of epicentral distance. The lines of best fit for the real and synthetic data correspond to those in Figures 5
178 and 6. Comparing the observed with synthetic data we find that in general, the observed PKiKP arrival is earlier than
179 predicted in the synthetics for AK135. There is a gradual decrease in observed differential time compared to predicted
180 differential time with increasing epicentral distance. This corresponds to a decrease in residuals with increasing depth
181 below the ICB.

182 Examining a map of the ray paths from the Indonesian event (Figure 8), we find that the paths with a more westerly
183 turning longitude have more positive residuals, indicating higher velocities in the inner core. As longitude becomes
184 more easterly, the residuals become less positive. This pattern remains consistent as latitude increases. We investigate
185 the relationship to both turning longitude and depth in Figure 9, which reveals that the more easterly turning data also
186 travel deeper into the inner core. Large positive residuals are observed at depths from 6 – 12 km. The residuals then
187 show a gradual decrease with increasing depth and turning longitude. At ~ 24 km depth, larger positive residuals are
188 found amongst the smaller values, indicating small scale variations.

189 We repeat our picking method for data from a further 12 events, using a combination of cross-correlation and
190 hand-picking to measure the relative arrival times of the peaks. Data from all events (Figure 10) also shows a general
191 decrease in residuals for ray paths with more easterly turning points. We find that there is also significant scatter in the
192 data in some regions, corroborating small scale variation. Here, we also note smaller and more negative residuals for
193 data with more northerly paths, suggesting some latitudinal variation in the velocity structure as well.

3.4. Velocity model

To quantify the potentially higher velocity in the uppermost layer, we make a simple layered 1D velocity model for our study area. The relationship between fractional travel time and velocity is used to calculate the seismic velocity structure from the differential travel time residuals, δt , as follows:

$$\frac{\delta t}{t_{AK135}} = \frac{\delta v}{v_{AK135}} \quad (2)$$

where t_{AK135} is the AK135 theoretical travel time for PKIKP in the inner core, v_{AK135} is the velocity in AK135, and δv is the velocity perturbation with respect to AK135.

Here, we calculate a two-layer velocity model for the inner core. The layers are defined by the PKIKP turning point, calculated using the TauP toolkit (Crotwell et al., 1999) with the AK135 reference Earth model. The epicentral distance ranges of $125 - 130^\circ$ and $130 - 135^\circ$ correspond to layers of approximately 6 – 17 km and 17 – 36 km below the ICB respectively. Since the seismic velocity in the upper layer affects the measured value of the residual in the lower layer, the velocity of the upper layer is calculated first. Subsequently, the influence of the velocity in the upper layer is determined and removed from data which turn in the lower layer. For this, we calculate the time spent in the upper layer and the corresponding contribution to the residual. The remaining perturbation is then attributed to the lower layer.

Using all of the data, we determine a mean value of $\frac{\delta t}{t}$ for each bin, and calculate the standard error on the mean as a measure of spread. Using Equation 2, we then calculate a two-layer velocity model for the region of the inner core studied (Figure 11). Table 2 contains the fractional residuals and our calculated velocities with errors, for all data and also for the Indonesia event alone. For the Indonesia event, we also calculate the velocity in the lower layer using the cross-correlation method, which is in excellent agreement with our new method.

We find that the velocity decreases with depth. The lower layer shows significant differences for all data versus the Indonesia event only; a clear indicator of regional variation in velocity structure. It is both lower in velocity, and has double the error for the lower layer. The larger error highlights the spread in residuals caused by including more data, and points to regional variation. The underlying velocity structure may be the result of a high velocity upper layer in the region (Attanayake et al., 2014). Alternatively, the observations may result from the inner core hemispheres, whereby the deeper ray paths spend more time in the low velocity west hemisphere, and latitudinal variation in the hemisphere boundary is reported (Cormier, 2015; Irving & Deuss, 2015; Yu et al, 2017). The lower velocity we detect in the northern part of our dataset may correspond to small scale mushy zones on the inner core boundary observed here (Tian & Wen, 2016; Shen et al., 2016).

4. Discussion

4.1. Method

Our new method to measure the PKIKP-PKiKP differential travel time at depths shallower than 15 km is successful up to depths of 6 km below the ICB. Consequently, we have made the first measurements of the very uppermost layer of the inner core, which opens up new possibilities for studying this region in future. Here, we have used paths which are predicted to primarily traverse the eastern hemisphere. As this area has a higher velocity, it means that PKIKP arrives earlier and the phases may be distinguished at shallower depths than for slower structure.

In order to confirm the validity of our method in the first instance, we compare our velocity model for depths below 15 km with a velocity model calculated for data which has been picked using cross-correlation. The results show good agreement (Table 2), indicating that our technique is sound for well-separated phases. This also shows the negligible influence of attenuation and broadening on the technique, for impulsive events.

The single and two-phase WKBJ synthetics are next used to determine the shortest epicentral distance at which we can apply our method for different velocity and attenuation models. This corresponds to the distance at which the PKIKP and PKiKP waveforms overlap to the extent that PKiKP affects the arrival time of PKIKP. For this test, we use synthetic data in the epicentral distance range 120 – 130°. We begin by aligning all of the synthetic data on the theoretical PKiKP peak travel time (as in Figure 5d). Using cross-correlation of the PKIKP and PKiKP characteristic peaks, we next measure the peak differential time for the single-phase PKIKP synthetics (Figure 5c) and the two-phase synthetics (Figure 5b).

As epicentral distance decreases, the waveforms begin to overlap. Hence, the two-phase results we obtained are similar to real data, whereas the single-phase measurements are the actual differential times between the peaks. The breakdown of our method therefore occurs where these measurements begin to diverge. It is expected that the distance limitations of our method will vary depending on velocity and attenuation of the inner core region sampled. The inner core velocity structure determines the PKIKP ray path through the inner core, as well as affecting travel time. A lower inner core velocity will result in the method breaking down at higher epicentral distances. Inner core attenuation acts as a filter to remove shorter period data, and may influence the maxima of the PKIKP peaks.

We explore the influence of different inner core and outer core velocity models, and the effect of inner core attenuation with Q of 200 for AK135. We firstly consider the epicentral distance at which the method breaks down. In Figure 12, the measurements for two-phase and single phase synthetics are shown in red and blue respectively. The point at which these two measurements diverge occurs can be seen at 125° for AK135 with and without attenuation. The results demonstrate that below 125°, the method cannot be applied, which justifies our decision to study stations at epicentral distances above 125°. Furthermore, attenuation with Q of 200 is observed to have negligible influence on the measurements. WKBJ synthetics incorporating attenuation (Figure S2) reveal that the major difference is the

254 amplitude and breadth of the PKIKP signal, and have little effect on the arrival time of the peak. Consequently, the
255 relative arrival times (Figure S3) are extremely similar to those without attenuation (Figure 7).

256 Corresponding measurements using PREM as a reference model show that the single-phase and two-phase mea-
257 surements diverge at a higher epicentral distance of around 128° . This is a result of the different ICB depth, and
258 different velocity in the upper inner core and lower outer core. Thus, the theoretical PKIKP-PKiKP differential times
259 are slightly smaller for PREM, producing larger residuals (Figure S4). The different velocity structure also alters the
260 distance at which the PKIKP and PKiKP waveforms merge (Figures S5, 5) and separate (Figures S6, 6). The change in
261 ICB impedance contrast affects their relative amplitudes, however this must also be considered in the context of inner
262 core attenuation. Structure in the lowermost outer core must also be considered. A reduced or increased velocity here
263 shifts the PKIKP-PKiKP residuals (Figure §7), and also affects the amplitude ratios of PKIKP and PKiKP depending
264 on the ICB impedance contrast. Since variations in the lowermost outer core are large-scale features (Cormier, 2009),
265 lateral structure will become relevant for global studies. On regional length scales, the different velocities act to shift
266 all the measurements, resulting in a relative shift in the calculated velocity model. This highlights the need for consid-
267 ering reference model, inner core ray path geometries, and regional velocity structure, when calculating the distance
268 at which the method breaks down. It is important to highlight that the velocity model we calculate is with respect to
269 the reference model used.

270 4.2. *Velocity structure*

271 Our calculated model has a higher velocity in the upper layer, however the ray paths in the two layers traverse
272 slightly different regions. One structure which could explain this is a high velocity lid in the region, with a lower
273 velocity closer to AK135 in the layer beneath. This is in agreement with previous observations of a high velocity layer
274 in the east hemisphere (Waszek & Deuss, 2011), although the thickness of the layers differs. A possible origin for this
275 structure is an enhanced lighter element concentration, caused by faster solidification in recent history (Aubert et al.,
276 2008).

277 Alternatively, since the deeper ray paths have more westerly turning points, the smaller residuals may be a con-
278 sequence of more time spent in the slower western hemisphere. This would require the hemisphere boundary to be
279 shifted westward in the shallow regions. The hemisphere boundary of 173°W determined by Waszek et al. (2011)
280 was calculated for data in the distance range $130 - 135^\circ$, and deeper data in the same study find a shift in the hemi-
281 sphere boundary eastwards with increasing depth. Our shallower data turn in the layer above this, and so a westward
282 shift would continue this trend. In this scenario, the western part of the paths are influenced by low velocity in the
283 western hemisphere. The shallowest paths travel much shorter distances in the western hemisphere, and therefore are
284 increasingly less affected as turning depth decreases. This produces increasingly positive residuals as turning depth
285 and longitude decreases, as observed.

We perform forward modelling using the 2.5D spectral element code AxiSEM (Nissen-Meyer et al., 2014) for the two possible velocity structures (Figure 13). We use data from the Indonesian event and the corresponding velocity values calculated for that event alone. For the high velocity lid model, we use a two-layer structure, where the upper layer extends to 16.3 km depth below the ICB. For the shifting boundary model, we introduce a hemispherical structure to the layers. In the upper layer, the boundary is placed at 175°E; in the lower layer, at 173°W. The latter value is taken from Waszek & Deuss (2011). The calculated velocities for the upper layer and/or east hemisphere is 11.142 km s⁻¹, and 11.011 km s⁻¹ for the lower layer and/or west hemisphere, introduced as a perturbation to AK135. For comparison, we first examine AxiSEM synthetics generated for AK135 (Figure S8). These synthetics display a broader waveform than WKBJ, although this does not significantly affect the arrival times. Small waveform differences to the AxiSEM seismograms generated for the updated models are noticeable in the PKIKP phases.

For each model, we obtained differential travel time residual measurements with respect to the observed data. Both models show an improvement in fit to the observations compared to AK135, revealed by much smaller travel time residuals (Figure 7). We find negligible difference between the two models, however. We perform the same layered inversion for the AxiSEM residuals as for the WKBJ AK135 residuals, in order to obtain percentage corrections to the input velocity structures. The results for each model overlap within error bounds of each other. For the hemispherical model, the corrections are $0.068 \pm 0.023\%$ in the upper layer, and $-0.52 \pm 0.23\%$ in the lower layer; the layered model has similar values of $0.066 \pm 0.023\%$ and $-0.55 \pm 0.24\%$. More advanced inversions are required to determine the true structure here; Figure 7b reveals that the updated velocity in the lower layer is slightly too high at short distances, and too low at large distances, requiring the addition of a positive velocity gradient.

Lateral variation must also be accounted for in such future work. Separately to the layered and/or hemispherical structure, we observe a decrease in residual with increasing latitude. This suggests the existence of regional variation within the eastern hemisphere, or movement in the hemisphere boundary with latitude. This is in agreement with previous studies which found complexity beneath the Pacific Ocean (Stroujkova & Cormier, 2004; Miller et al., 2013; Cormier, 2015; Irving & Deuss, 2015; Yu et al, 2017). The inner core boundary beneath the northern Pacific Ocean is also found to display small scale features including topography and melting (Waszek & Deuss, 2015; Tian & Wen, 2016; Shen et al., 2016).

4.3. Future work

The application of our new method to these events acts as proof of concept, showing that the compressional wave velocity of the inner core at depths as shallow as 6 km below the ICB can be measured. This reveals the potential to constrain regional velocity structure here. The high density of ray paths highlights the implications of this method for mapping small scale structure in the uppermost inner core as well as lowermost outer core, to be performed in future studies using sophisticated inversion techniques. Insight into properties of the uppermost inner core is essential

318 to understand heat transport processes across the ICB (Gubbins et al., 2011), and seismic properties may be linked to
319 localised freezing and melting of the inner core boundary (Cormier, 2015).

320 **5. Conclusions**

321 We have successfully developed a method to measure the compressional wave velocity in the uppermost inner
322 core, using waveform comparison between observed and synthetic data. We show that by measuring different parts of
323 the combined PKIKP and PKiKP waveform, we can obtain differential travel time residuals at much shorter epicentral
324 distances than previously used. This allows the velocity at depths shallower than 15 km to be determined, which had
325 not previously been isolated from paths which sample it. As proof of concept we apply our method to an event with
326 inner core ray paths which cross the Pacific hemisphere boundary, and compile data from further events sampling
327 this region. We find evidence for either a high velocity upper layer, or a westward shift in the hemisphere boundary
328 in the upper layer, and further regional variation. Forward modelling shows that both layering or hemispheres are
329 equally adequate to explain our general observations; more advanced inversion techniques are the next step to map the
330 detailed properties. Our study provides a new technique to study the upper layers of the inner core, which will help to
331 determine the origin of its complex features.

332 **Acknowledgments**

333 HG is funded by the Natural Environment Research Council Doctoral Training Partnership in Environmental Re-
334 search at the University of Oxford. LW is the recipient of a Discovery Early Career Research Award (project number
335 DE170100329) funded by the Australian Government. AD was funded by the European Research Council (ERC)
336 under the European Unions Horizon 2020 research and innovation programme (grant agreement no. 681535 ATUNE),
337 a Vici award (number 016.160.310/526) from the Netherlands organization for scientific research (NWO) and an
338 Ammodo-KNAW award in Natural Sciences. We thank Vernon Cormier, Satoru Tanaka, and an anonymous reviewer
339 for helpful and constructive comments. The facilities of the IRIS Data Management System, and specifically the
340 IRIS Data Management Center, were used for access to waveform and metadata required in this study. The IRIS
341 DMS is funded through the National Science Foundation and specifically the GEO Directorate through the Instru-
342 mentation and Facilities Program of the National Science Foundation under Cooperative Agreement EAR-1063471
343 (<http://www.iris.edu/wilber3/>).

6. Figure Captions

1. PKIKP (blue) and PKiKP (red) ray paths from an event at a depth of 265.7 km to a station at an epicentral distance of 132.5° .
2. Map showing inner core ray paths (black lines) to stations at epicentral distances between 125° and 135° from the Indonesian event on 15 November 2011 (red star). The yellow circle on the inner core path marks the turning point. The thick vertical black line is the location of the hemisphere boundary proposed by Waszek and Deuss (2011), at 173° W at depths of 15 – 30 km inside the inner core.
3. Observed (left) and synthetic (right) seismograms recorded at stations at epicentral distances from 125° to 135° from the source, plotted using reduced velocity. PKIKP and PKiKP arrival times as predicted by TauP are shown. Note that these predicted times are the onset of the phases; for picking, we align to the phase maxima.
4. Seismograms with epicentral distances of (a) 125.6° and (b) 134.6° . PKIKP and PKiKP are indicated by arrows for the larger epicentral distance. At the shorter epicentral distance, the arrows indicate the peaks we use to identify the phases.
5. Seismograms aligned to PKiKP in the 125° - 130° epicentral distance range. (a) Observed data, (b) Synthetic data for PKIKP and PKiKP, (c) Synthetic data for PKIKP only, (d) Synthetic data for PKiKP only. The red line marks the position of the highest peak, corresponding to PKiKP. The peak marked by the blue lines corresponds to the arrival of PKIKP. These lines were plotted by measuring the peak position in each seismogram and taking a best fit line through these points using least-squares regression (Williams & Kelley, 2011).
6. Seismograms aligned to PKiKP in the 130° - 135° epicentral distance range. (a) Observed data, (b) Synthetic data, PKIKP and PKiKP, (c) Synthetic data, PKIKP only, (d) Synthetic data, PKiKP only. The peaks marked with a red line in correspond to the arrival of PKiKP. The peaks marked with a blue line correspond to the second peak in the PKIKP waveform. Again, the blue lines are plotted by calculating a best fit line through the measured peak positions using least-squares regression (Williams & Kelley, 2011).
7. The positions of the peaks corresponding to PKIKP and PKiKP as a function of epicentral distance. (a) 125° – 130° , (b) 130° – 135° . The observed PKiKP data are shown in light blue, and the WKB synthetic data for AK135 in dark blue. Our calculated best fitting two-layer model is in green. The PKiKP peak is at 0 s. The PKIKP-PKiKP differential increases with increasing epicentral distance. The best fit lines were calculated by least-squares regression (Williams & Kelley, 2011), and are the same lines as were plotted on the aligned seismograms in Figures 5 and 6. The errors for each data point are calculated from the standard error on 300 random resamples of the dataset for the average discrepancy between the actual measurement and best fit line. This is 0.09 s for the real data and 0.01 s for the synthetic data.
8. The fractional differential travel time residual displayed at the PKIKP turning point for data from the 15 Novem-

ber 2011 Indonesia event. Inner core ray paths are shown as black lines.

9. Fractional differential travel time as a function of PKIKP turning point and turning longitude for all data. As the longitude and depth increase, the fractional differential travel time becomes more positive.
10. The fractional differential travel time residual displayed at the PKIKP turning point for all data. Inner core ray paths are shown as black lines.
11. Two-layer velocity model calculated from the data. AK135 is shown in blue, while the black line is the updated velocity model. The grey shading represents the uncertainty in the updated velocity model.
12. The differential time between characteristic PKIKP and PKiKP peaks for single-phase (blue) and two-phase (red) WKBJ synthetics. (a) AK135. (b) AK135 with attenuation of $Q=200$. (c) PREM.
13. Synthetic seismograms generated using AxiSEM, aligned to PKiKP in the 125° - 135° epicentral distance range. (a,b) Hemispherical model, (c,d) Layered model. The red line marks the position of the highest peak, corresponding to PKiKP. The peak marked by the blue lines corresponds to the arrival of PKIKP. These lines were plotted by measuring the peak position in each seismogram and taking a best fit line through these points using least-squares regression (Williams & Kelley, 2011).

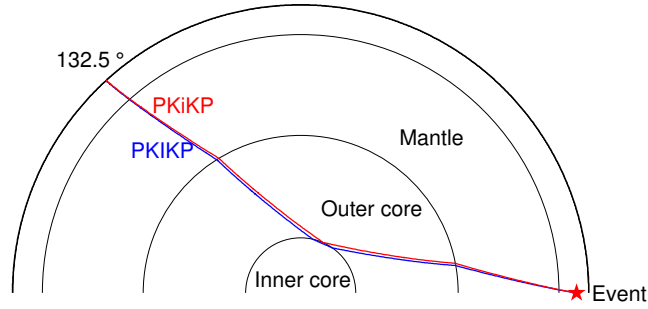


Figure 1: PKIKP (blue) and PKiKP (red) ray paths from an event at a depth of 265.7 km to a station at an epicentral distance of 132.5° .

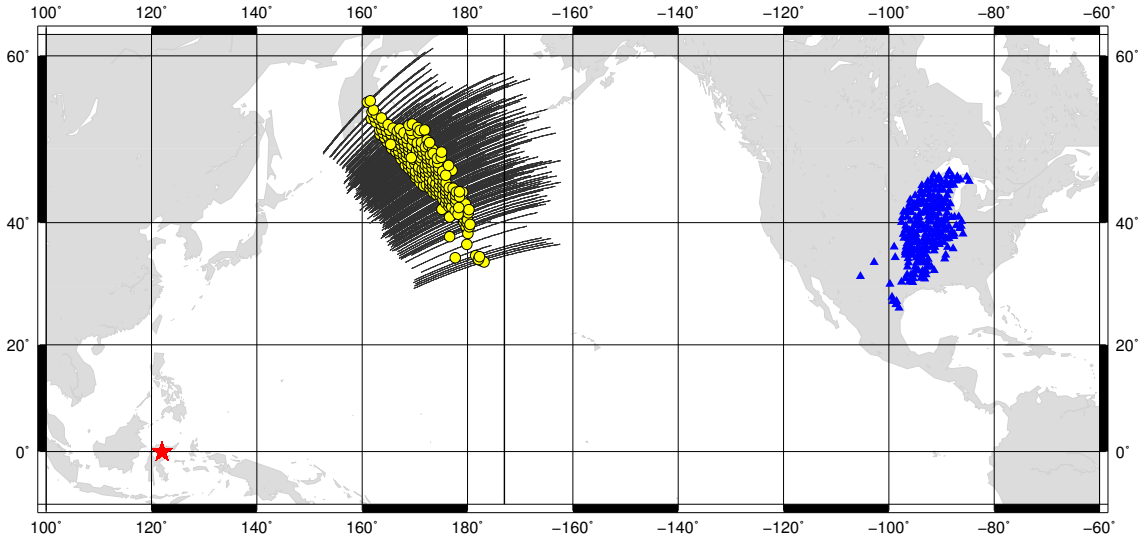


Figure 2: Map showing inner core ray paths (black lines) to stations at epicentral distances between 125° and 135° from the Indonesian event on 15 November 2011 (red star). The yellow circle on the inner core path marks the turning point. The thick vertical black line is the location of the hemisphere boundary proposed by Waszek and Deuss (2011), at 173°W at depths of 15–30 km inside the inner core.

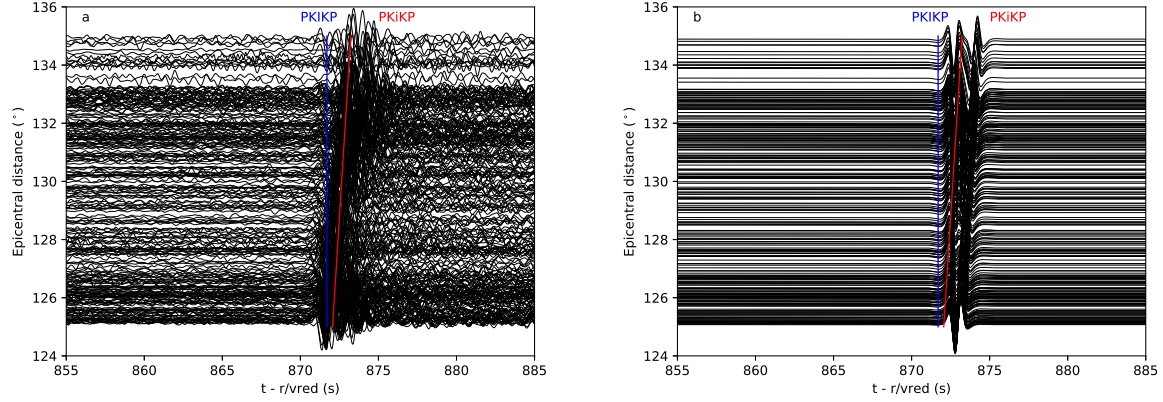


Figure 3: Observed (left) and synthetic (right) seismograms recorded at stations at epicentral distances from 125° to 135° from the source, plotted using reduced velocity. PKIKP and PKiKP arrival times as predicted by TauP are shown. Note that these predicted times are the onset of the phases; for picking, we align to the phase maxima.

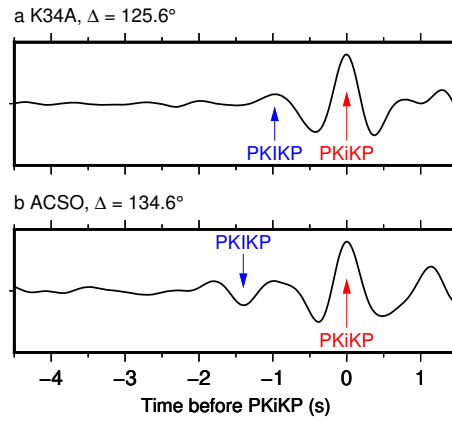


Figure 4: Seismograms with epicentral distances of (a) 125.6° and (b) 134.6° . PKIKP and PKiKP are indicated by arrows for the larger epicentral distance. At the shorter epicentral distance, the arrows indicate the peaks we use to identify the phases.

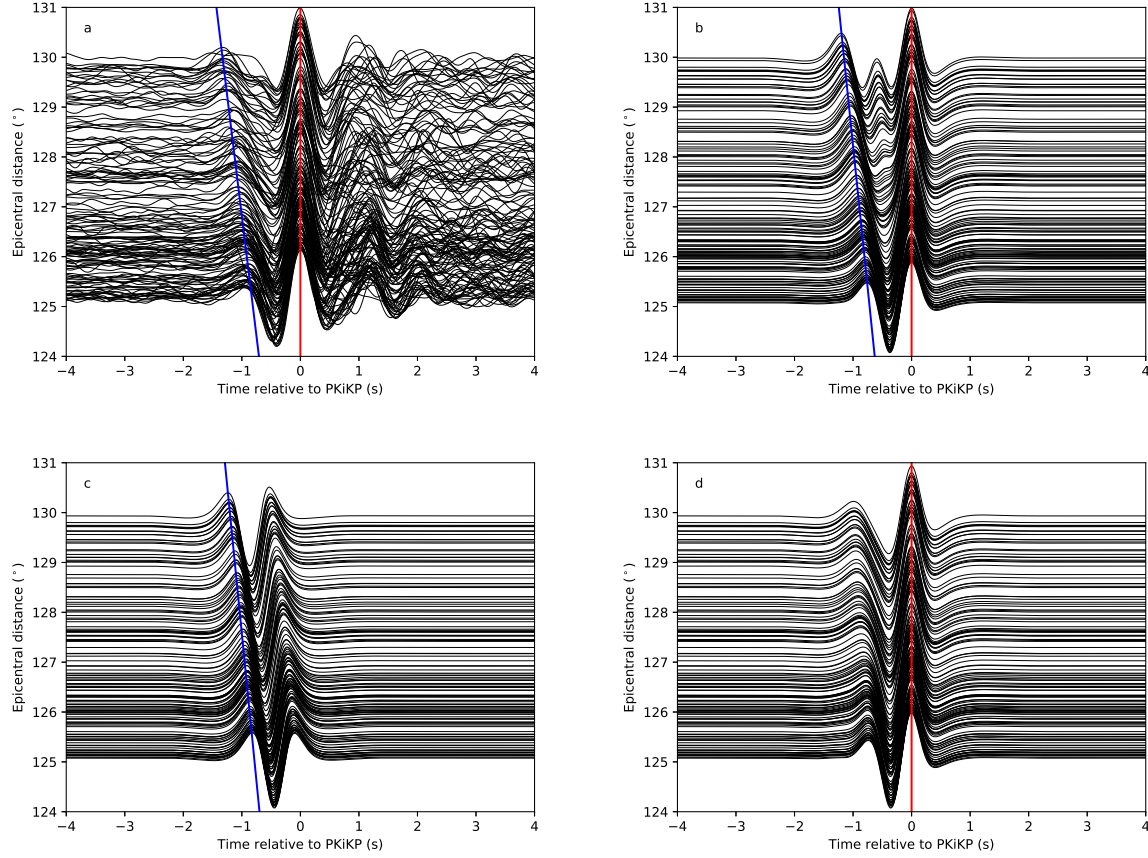


Figure 5: Seismograms aligned to PKiKP in the 125° - 130° epicentral distance range. (a) Observed data, (b) Synthetic data for PKiKP and PKiKP, (c) Synthetic data for PKiKP only, (d) Synthetic data for PKiKP only. The red line marks the position of the highest peak, corresponding to PKiKP. The peak marked by the blue lines corresponds to the arrival of PKiKP. These lines were plotted by measuring the peak position in each seismogram and taking a best fit line through these points using least-squares regression (Williams & Kelley, 2011).

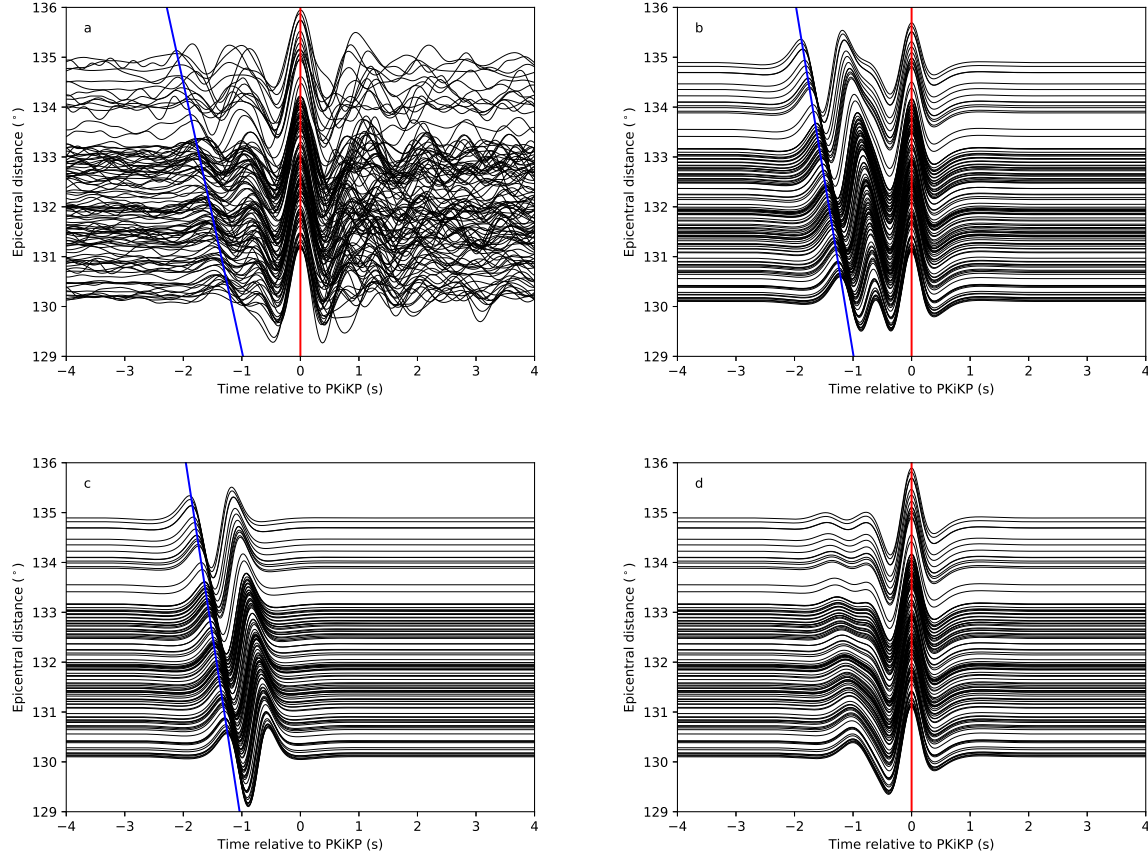


Figure 6: Seismograms aligned to PKiKP in the 130° - 135° epicentral distance range. (a) Observed data, (b) Synthetic data, PKiKP and PKiKP, (c) Synthetic data, PKiKP only, (d) Synthetic data, PKiKP only. The peaks marked with a red line in correspond to the arrival of PKiKP. The peaks marked with a blue line correspond to the second peak in the PKiKP waveform. Again, the blue lines are plotted by calculating a best fit line through the measured peak positions using least-squares regression (Williams & Kelley, 2011).

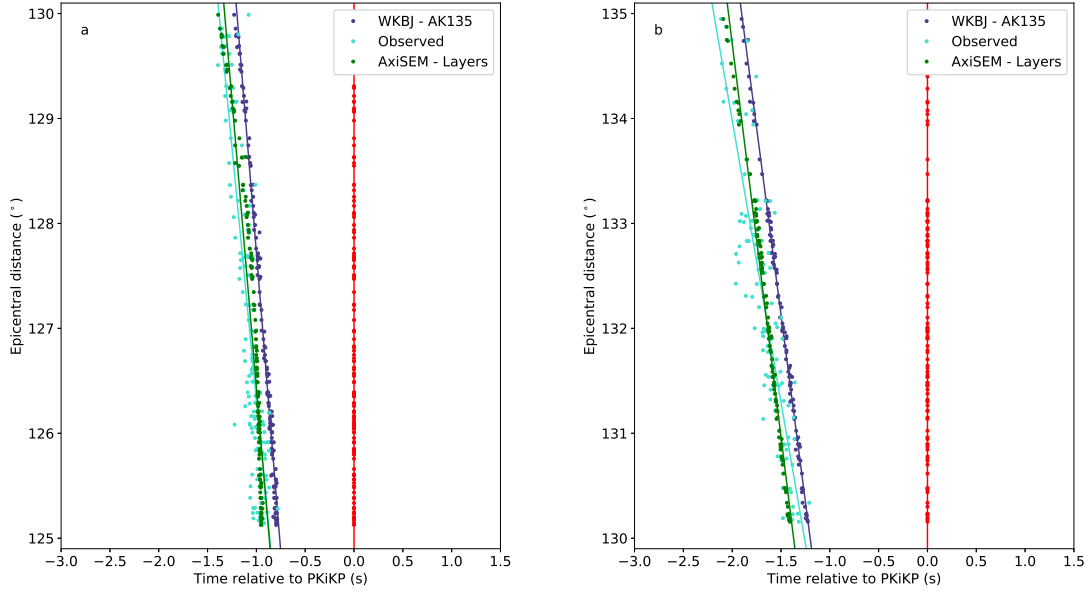


Figure 7: The positions of the peaks corresponding to PKiKP and PKiKP as a function of epicentral distance. (a) $125 - 130^\circ$, (b) $130 - 135^\circ$. The observed PKiKP data are shown in light blue, and the WKBJ synthetic data for AK135 in dark blue. Our calculated best fitting two-layer model is in green. The PKiKP peak is at 0 s. The PKiKP-PKiKP differential increases with increasing epicentral distance. The best fit lines were calculated by least-squares regression (Williams & Kelley, 2011), and are the same lines as were plotted on the aligned seismograms in Figures 5 and 6. The errors for each data point are calculated from the standard error on 300 random resamples of the dataset for the average discrepancy between the actual measurement and best fit line. This is 0.09 s for the real data and 0.01 s for the synthetic data.

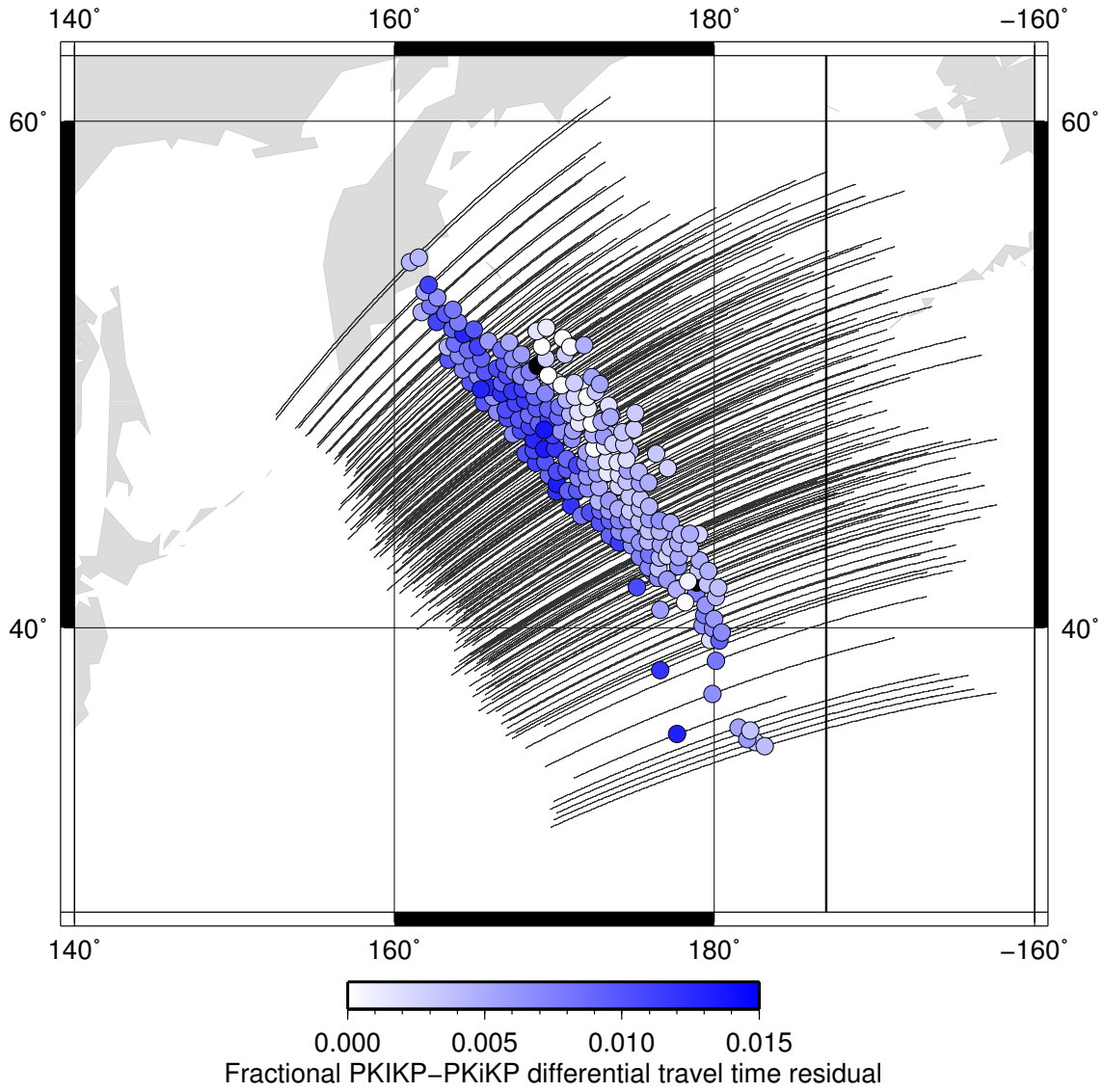


Figure 8: The fractional differential travel time residual displayed at the PKIKP turning point for data from the 15 November 2011 Indonesia event. Inner core ray paths are shown as black lines.

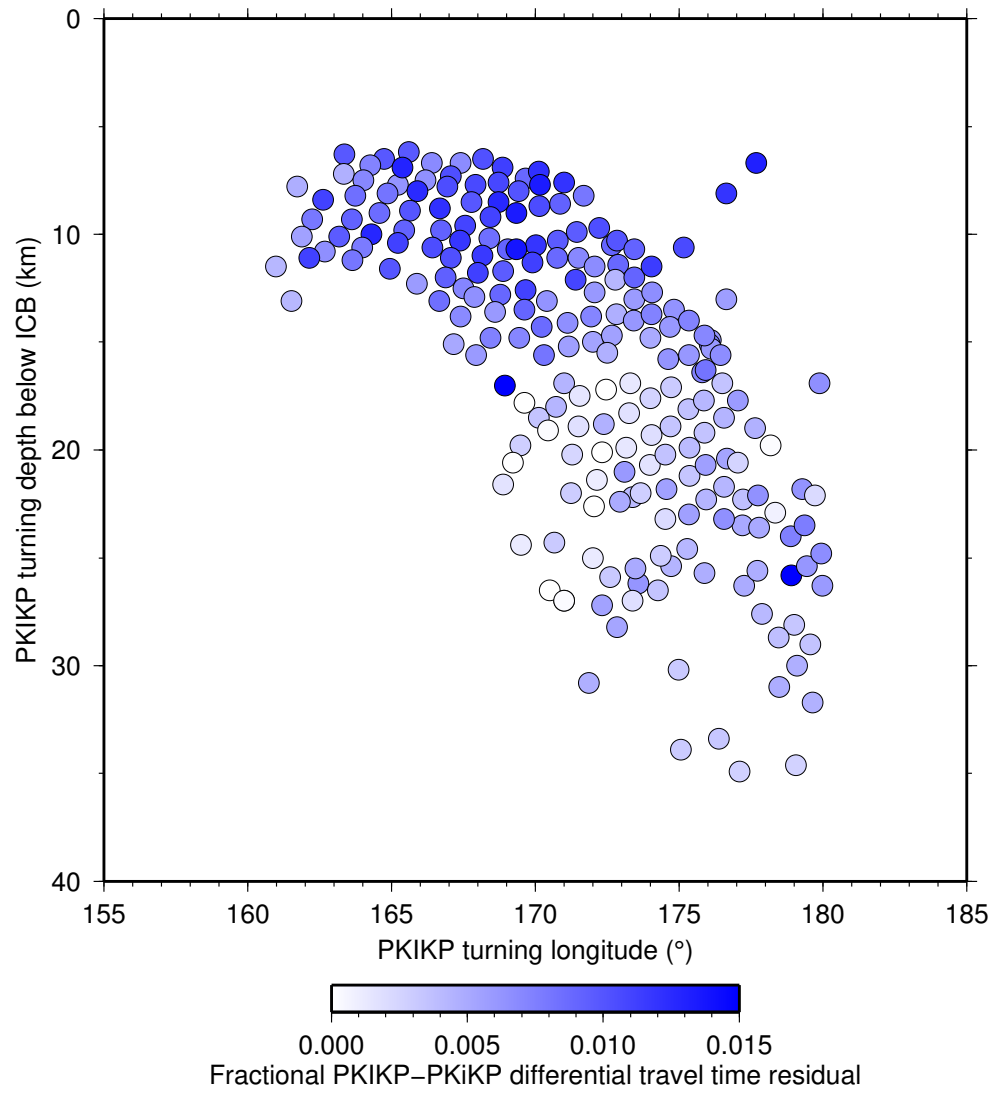


Figure 9: Fractional differential travel time as a function of PKIKP turning point and turning longitude for all data. As the longitude and depth increase, the fractional differential travel time becomes more positive.

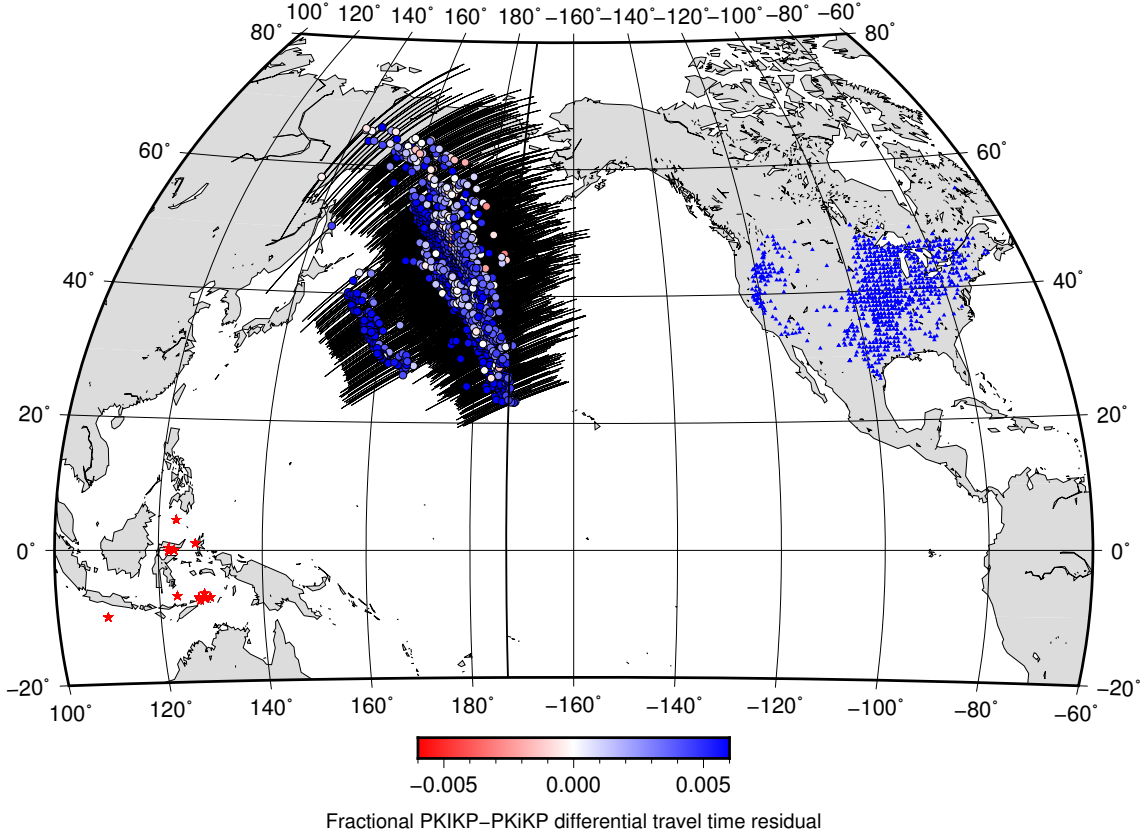


Figure 10: The fractional differential travel time residual displayed at the PKIKP turning point for all data. Inner core ray paths are shown as black lines.

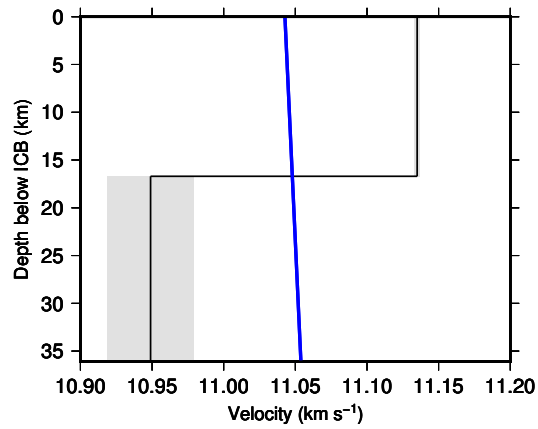


Figure 11: Two-layer velocity model calculated from the data. AK135 is shown in blue, while the black line is the updated velocity model. The grey shading represents the uncertainty in the updated velocity model.

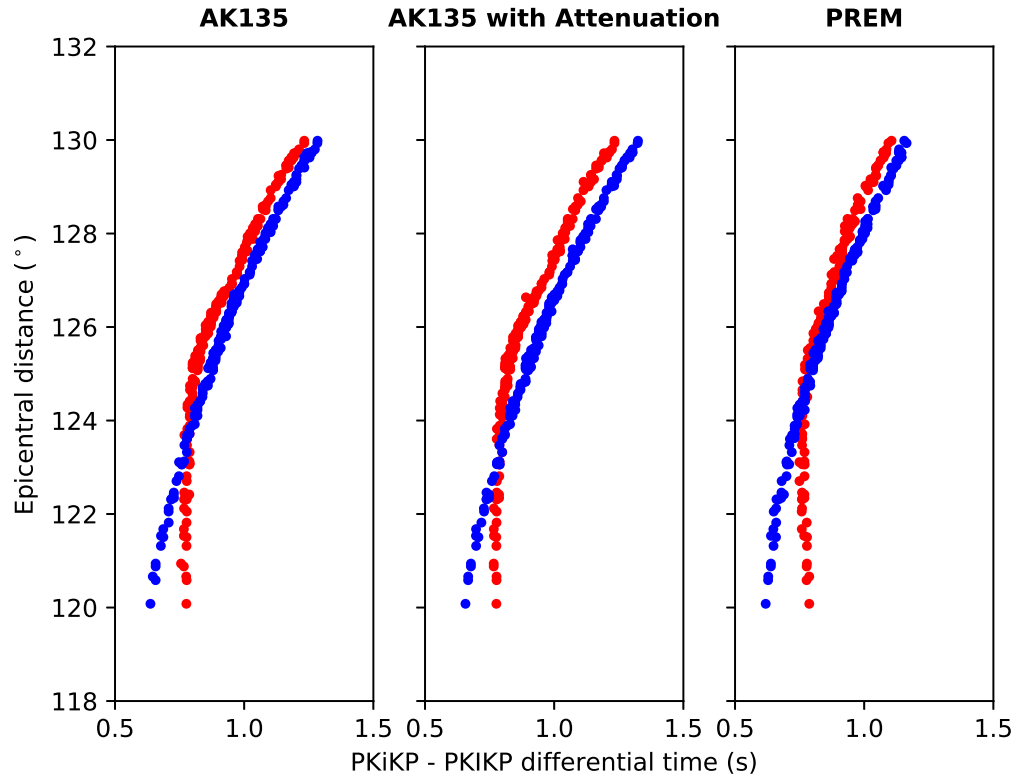


Figure 12: The differential time between characteristic PKiKP and PKiKP peaks for single-phase (blue) and two-phase (red) WKBJ synthetics. (a) AK135. (b) AK135 with attenuation of $Q=200$. (c) PREM.

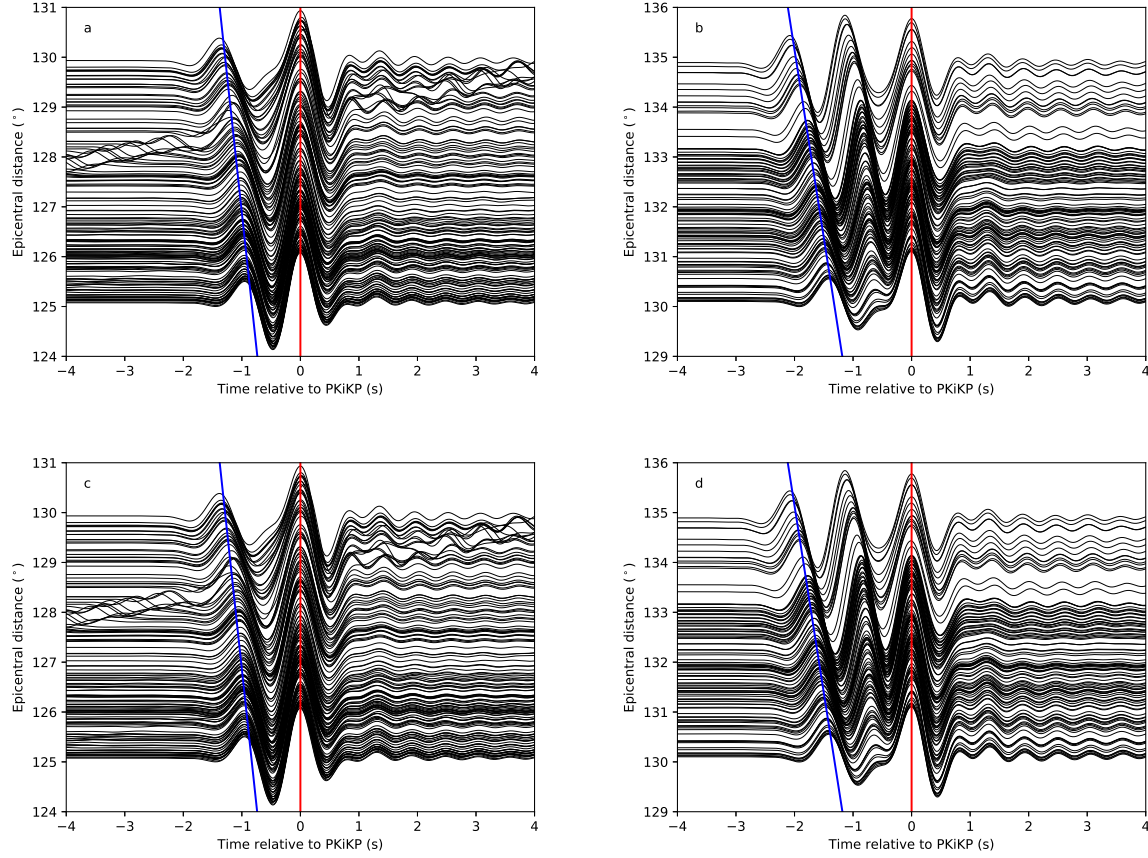


Figure 13: Synthetic seismograms generated using AxiSEM, aligned to PKiKP in the 125° - 135° epicentral distance range. (a,b) Hemispherical model, (c,d) Layered model. The red line marks the position of the highest peak, corresponding to PKiKP. The peak marked by the blue lines corresponds to the arrival of PKiKP. These lines were plotted by measuring the peak position in each seismogram and taking a best fit line through these points using least-squares regression (Williams & Kelley, 2011).

Table 1: List of events used in this study

Date	Latitude ($^{\circ}$)	Longitude ($^{\circ}$)	Depth (km)	Magnitude (M_b)
19 January 2007	-10.0	109.7	38.3	5.9
15 February 2010	-7.3	128.8	136.2	6.3
2 October 2010	-6.6	128.7	243.3	5.3
15 December 2010	-7.5	128.8	147.3	5.8
16 July 2011	-7.2	127.6	259.9	5.8
15 November 2011	-7.6	127.8	176.8	5.8
15 November 2011 (2)	-0.1	121.9	265.7	5.7
13 December 2011	0.0	123.1	164.4	6.3
11 January 2012	-6.9	123.3	652.7	5.2
27 June 2013	1.1	127.1	139.6	5.8
12 August 2013	-7.1	129.8	105.2	6.1
3 November 2013	4.7	123.3	543.1	6.0
28 March 2015	0.4	122.0	130.6	5.9

Table 2: Results from updating the velocity model

Data	Epicentral distance ($^{\circ}$)	$\delta t/t$	$v_{new}/\text{km s}^{-1}$
All data	125 – 130	0.0082 ± 0.0002	11.137 ± 0.002
All data	130 – 135	-0.0092 ± 0.0031	10.949 ± 0.032
Indonesia event only	125 – 130	0.0086 ± 0.0002	11.142 ± 0.002
Indonesia event only	130 – 135	-0.0036 ± 0.0015	11.011 ± 0.017
Indonesia event, cross-correlation	130 – 135	-0.0029 ± 0.0014	11.018 ± 0.016

References

- Alboussière, T., Deguen, R. & Melzani, M., 2010. Melting-induced stratification above the Earth's inner core due to convective translation. *Nature*, 466:744–747.
- Antonangeli, D., Siebert, J., Badro, J., Farber, D., Fiquet, G., Morard, G. & Ryerson, F., 2010. Composition of the Earth's inner core from high-pressure sound velocity measurements in Fe-Ni-Si alloys. *Earth and Planetary Science Letters*, 295:292 – 296.
- Attanayake, J., Cormier, V. & de Silva, S., 2014. Uppermost inner core seismic structure – new insights from body waveform inversion. *Earth. Planet. Sci. Lett.*, 385:49–58.
- Aubert, J., Amit, H., Hulot, G. & Olson, P., 2008. Thermochemical flows couple the Earth's inner core growth to mantle heterogeneity. *Nature*, 454:758–762.
- Cao, A. & Romanowicz, B., 2004. Hemispherical transition of seismic attenuation at the top of the Earth's inner core. *Earth Planet. Sci. Lett.*, 228:243–253.
- Cao, A. & Romanowicz, B., 2006. Short wavelength topography on the inner-core boundary. *Proc. Nat. Acad. Sci.*, 104:31–35.
- Chapman, C., 1976. A first motion alternative to geometrical ray theory. *Geophys. Res. Lett.*, 3:153–156.
- Cormier, V., 1999. Anisotropy of heterogeneity scale lengths in the lower mantle from PKIKP precursors. *Geophys. J. Int.*, 136:373–384.
- Cormier, V., 1999. A glassy lowermost outer core. *Geophys. J. Int.*, 179:374–380.
- Cormier, V., 2015. Detection of inner core solidification from observations of antipodal PKIKP. *Geophys. Res. Lett.*, 42:7459–7466.
- Creager, K., 1999. Large-scale variations in inner core anisotropy. *Journal of Geophysical Research*, 104:23127 – 23139.
- Creager, K., 1992. Anisotropy of the inner core from differential travel times of the phases PKP and PKIKP. *Nature*, 356:309–314.
- Crotwell, H., Owens, T. & Ritsema, J., 1999. The TauP Toolkit: flexible seismic travel-time and raypath utilities. *Seismol. Res. Lett.*, 70:154–160.
- Deuss, A., Irving, J. & Woodhouse, J., 2010. Regional variation of inner core anisotropy from seismic normal mode observations. *Science.*, 328:1018–1020.

Ekström, G., Nettles, M. & Dziewoński, A.M., 2012. Centroid-moment tensors for 13,017 earthquakes. *Physics of the Earth and Planetary Interiors*, 200-201:1–9.

Garcia, R. & Souriau, A., 2000. Inner core anisotropy and heterogeneity level. *Geophys. Res. Lett.*, 27:3121–3124.

Garcia, R., 2002. Constraints on upper inner-core structure from waveform inversion of core phases. *Geophys. J. Int.*, 150:651–664.

Geballe, Z., Lasbleis, M., Cormier, V. and Day, E., 2013. Sharp hemisphere boundaries in a translating inner core. *Geophys. Res. Lett.*, 40:1719–1723.

Gubbins, D., Sreenivasan, B., Mound, J. and Rost, S. 2011. Melting of the Earth’s inner core. *Nature*, 473:361–363.

Irving, J. & Deuss, A., 2011. Hemispherical structure in inner core velocity anisotropy. *J. Geophys. Res.*, 116: 2156–2202.

Irving, J. & Deuss, A., 2015. Regional seismic variations in the inner core under the North Pacific. *Geophys. J. Int.*, 203:2189–2199.

Kennett, B., Engdahl, E. & Buland, R., 1995. Constraints on seismic velocities in the Earth from travel times. *Geophys. J. Int.*, 122:108–124.

Jacobs, J., 1953. The Earth’s inner core. *Nature*, 172:297 – 298.

Labrosse, S., Poirier, J. and Le Mouél, J., 2001. The age of the inner core. *Earth. Planet. Sci. Lett.*, 190:111 – 123.

Love, A., 1927. A Treatise on the Mathematical Theory of Elasticity. *Cambridge Univ. Press, New York*

Miller, M., Niu, F., & Vanacore, E., 2013. Lopsided growth of Earth’s inner core. *Science*, 328:1014–1017.

Monnereau, M., Calvet, M., Margerin, L. & Souriau, A., 2010. Aspherical structural heterogeneity within the upper-most inner core: Insights into the hemispherical boundaries and core formation *Phys. Earth. Planet. Inter.*, 101: 131–156.

Morelli, A., Dziewonski, A. & Woodhouse, J., 1986. Anisotropy of the inner core inferred from PKIKP travel times. *Geophys. Res. Lett.*, 13:1545–1548.

Niu, F. & Wen, L., 2001. Hemispherical variations in seismic velocity at the top of the Earth’s inner core. *Nature*, 410:1081–1084.

Nissen-Meyer, T., van Driel, M., Stähler, S., Hosseini, K., Hempel, S., Auer, L., Colombi, A. & Fournier, A., 2014. AxiSEM: broadband 3-D seismic wavefields in axisymmetric media. *Solid Earth*, 5:423–445.

446 Oreshin, S. and Vinnik, L. 2004. Heterogeneity and anisotropy of seismic attenuation in the inner core. *Geophys. Res.*
 447 *Lett.*, 31:2613–2616.

448 Ouzounis, A. & Creager, K., 2001. Heterogeneity and anisotropy of seismic attenuation in the inner core. *Geophys.*
 449 *Res. Lett.*, 28:4331–4334.

450 Poupinet, G., Pillet, R. & Souriau, A., 1983 Possible heterogeneity of the Earth's core deduced from PKIKP travel
 451 times. *Nature*, 305:204–206.

452 Shen, Z., Ai, Y., He., Y. & Jiang, M., 2016. Using pre-critical PKiKP-PcP phases to constrain the regional structures
 453 of the inner core boundary beneath East Asia. *Phys. Earth. Planet. Inter.*, 252:37–48.

454 Song, X. & Helmberger, D., 1998. Seismic evidence for an inner core transition zone. *Science*, 282:924–927.

455 Stroujkova, A. & Cormier, V., 2004. Regional variations in the uppermost 100 km of the Earth's inner core. *J.*
 456 *Geophys. Res.*, 109:B10307.

457 Sumita, I. & Olson, P., 1999. A laboratory model for convection in Earth's core driven by a thermally heterogeneous
 458 mantle. *Science*, 286:1547–1549.

459 Sun, X. & Song, X., 2008. Tomographic inversion for three-dimensional anisotropy of Earth's inner core. *Phys. Earth*
 460 *Planet. Inter.*, 167:53–70.

461 Tanaka, S. & Hamaguchi, H. 1997. Degree one heterogeneity and hemispherical variation of anisotropy in the inner
 462 core from PKP(BC) - PKP(DF) times. *J. Geophys. Res.*, 102:2925–2938.

463 Tian, D. & Wen, L., 2016. Seismological evidence for a localized mushy zone at the Earth's inner core boundary. *Nat.*
 464 *Comms.*, 8:165.

465 Thomas, C., Kendall, J. & Helffrich, G., 2009. Probing two low-velocity regions with PKP b-caustic amplitudes and
 466 scattering. *Geophys. J. Int.*, 178:503–512.

467 Waszek, L., Irving, J. & Deuss, A., 2011. Reconciling the hemispherical structure of Earth's inner core with its
 468 super-rotation. *Nature Geosci.*, 4:264–267.

469 Vinnik, L., Romanowicz, B. & Breger, L., 1994. Anisotropy in the center of the inner core. *Geophys. Res. Lett.*, 21:
 470 1671–1674.

471 Waszek, L. & Deuss, A., 2011. Distinct layering in the hemispherical seismic velocity structure of Earth's upper inner
 472 core. *J. Geophys. Res.*, 116:12313–12326.

473 Waszek, L. & Deuss, A., 2015. Anomalously strong observations of PKiKP/PcP amplitude ratios on a global scale. *J.*
474 *Geophys. Res.*, 120:5175–5190.

475 Wen, L. & Niu, F., 2002. Seismic velocity and attenuation structures in the top of the Earth's inner core. *J. Geophys.*
476 *Res.*, 107:B11, 2273.

477 Woodhouse, J., Giardini, D. & Li, X., 1986. Evidence for inner core anisotropy from free oscillations. *Geophys. Res.*
478 *Lett.*, 13:1549–1552.

479 Williams, T. & Kelley, C., 2011. Gnuplot 4.5: an interactive plotting program. <http://gnuplot.info>.

480 Yee, T., Rhie, J. and Tkalčić, H., 2014. Regionally heterogeneous uppermost inner core observed with Hi-net array. *J.*
481 *Geophys. Res.*, 119:7823–7845.

482 Yu, W. & Wen, L., 2007. Complex seismic anisotropy in the top of the Earth's inner core beneath Africa. *J. Geophys.*
483 *Res.*, 112:B08304, doi:10.1029/2006JM004868.

484 Yu, W., Su, J., Song, T., Huang, H., Mozziconacci, L. and Huang, B., 2017. The inner core hemispheric boundary near
485 180°W. *Phys. Earth. Planet. Inter.*, 272:1–16.